Check for updates

Advanced Materials

ADVANCED MATERIALS
www.advmat.de

RESEARCH ARTICLE

Micron-Textured Ambipolar Photodetectors Enabling ~20 µs Photonic Adaptation

Tingting Yan[1] | Yarong Gu[1] | Bobo Li[2] | Ming Deng[1] | Zijin Zhao[1] | Ziqing Li[3] | Junhao Chu[3] | Limin Wu[1,4] | Xiaosheng Fang[1]

[1]College of Smart Materials and Future Energy, State Key Laboratory of Molecular Engineering of Polymers, Fudan University, Shanghai, P. R. China | [2]School of Cyber Science and Engineering, Wuhan University, Wuhan, P. R. China | [3]State Key Laboratory of Photovoltaic Science and Technology, Shanghai Frontiers Science Research Base of Intelligent Optoelectronics and Perception, Institute of Optoelectronics, Fudan University, Shanghai, P. R. China | [4]College of Chemistry and Chemical Engineering, Inner Mongolia University, Hohhot, P. R. China

Correspondence: Limin Wu (lmw@fudan.edu.cn) | Xiaosheng Fang (xshfang@fudan.edu.cn)

Received: 23 July 2026 | **Revised:** 1 September 2026 | **Accepted:** 15 September 2026

Keywords: ambipolar photodetectors | bulk-heterojunctions | flexible optoelectronics | interfacial engineering

ABSTRACT

The rapid development of artificial intelligence calls for compact, flexible, and intelligent photodetectors. However, strong background illumination can overwhelm weak optical signals, while downstream compensation imposes substantial computational burdens, thereby introducing considerable processing latency. Here, we demonstrate an ultrathin (8 µm), mechanically flexible ambipolar electronic vision (AEV) system that suppresses background optical interference directly at the photodetection front end. Symmetric back-to-back Schottky barriers minimize the net vertical internal electric field, while a self-assembled donor-enriched micron-scale texture generates a small surface-potential gradient (~10 mV) to balance carrier transport and collection. This mechanism stabilizes illumination-direction-dependent photocurrent polarity near zero bias, reduces the minimum irradiance required for ambipolar operation from 175 mW cm^{-2} to 0.1 mW cm^{-2}, corresponding to an approximately 1750-fold reduction. Through the device-level superposition of oppositely signed photocurrents, the ultrathin, flexible AEV array directly suppresses background-induced photocurrent offsets and exhibits bidirectional response times of ~20 µs, enabling rapid photonic adaptation. The ambipolar response remains stable after array integration and 3500 bending cycles. Nearly 100% recognition accuracy is maintained under strong background illumination of ~11 mW cm^{-2}, establishing a device-level strategy for rapid and reliable visual perception in flexible and conformable electronic vision systems.

1 | Introduction

Conventional photodiodes typically rely on external compensation techniques, such as lock-in amplification, to approach background-limited detection [1, 2]. However, their active circuitry increases power consumption and system complexity, thereby imposing critical constraints for miniaturized systems. More fundamentally, although generating both electrons and holes, the fixed built-in electric field in conventional photodiodes enforces a single-polarity photoresponse, resulting in strictly unidirectional charge transport. This inherent unipolarity leads to the loss of spatiotemporal information in incident light, thereby imposing critical limitations of sensor–processor dichotomy and dynamic response hysteresis.

Artificial retina systems have been developed to overcome these physical limitations and achieve closed-loop intelligent systems that integrate sensing and computation [3–9]. Central to this paradigm are ambipolar photodetectors with dynamically reversible photoresponse polarity, which actively control the

All rights reserved, including rights for text and data mining and training of artificial intelligence technologies or similar technologies.
© 2026 Wiley-VCH GmbH

direction of photocurrent flow (positive/negative response) [10–14]. By modulating their response polarity through external stimulation such as bias voltage, light intensity, or gate voltage [15–18], these devices transcend the unipolar operational constraints of conventional photodetectors. Critically, the device-level superposition of positive and negative photocurrents enables complementary optical inputs to be encoded within a single electrical signal channel, allowing background-offset suppression and differential preprocessing directly at the photoelectric interface. This establishes a sensor-level preprocessing strategy whose response speed is primarily governed by intrinsic photoelectric processes [12, 19, 20]. It thereby offers significant potential for advancing adaptive, energy-efficient intelligent perception technologies.

Parallel advances in emerging photodetector technologies [6, 21–27], particularly in low-dimensional and organic semiconductors, have delivered ultrathin structures, broadband spectral response, and low power consumption with high-responsivities spanning from the ultraviolet to terahertz bands have been achieved [28–32]. These developments provide a crucial materials and device foundation for flexible optoelectronics and bio-inspired vision systems with vision-inspired perceptual capabilities. As core modules in optical information processing, ambipolar photodetectors encode multidimensional optical information (including intensity, wavelength, and polarization) into processable electrical signals via tailed photoelectric conversion pathways [33–38].

Nevertheless, persistent challenges remain in high-ambient-light environments, where steady intense illumination can mask weak target signals, while abrupt illumination changes degrade image signal-to-noise ratio (SNR), reduce resolution, weaken target contrast, and blurs contours. In most artificial vision systems, including current commercial imaging technologies and artificial retina devices, bright adaptation to such illumination transients remains slow or incomplete, as it is primarily addressed at the circuit or algorithm level rather than intrinsically at the photodetector level [39, 40]. Such prolonged light-adaptation times severely constrain real-time visual processing and in-sensor image preprocessing. In parallel, the intrinsic mechanical flexibility of ambipolar photodetectors remains restricted by material systems and device architectures, impeding their integration into deformable and wearable vision platforms.

Here, we demonstrate an ultrathin (8 μm), mechanically flexible ambipolar electronic vision (AEV) system that suppresses background optical interference directly at the photodetection front end. By integrating symmetric back-to-back Schottky barriers with a self-assembled donor-enriched micron-scale texture, the device minimizes the net vertical electric field while generating a small surface-potential gradient (~10 mV) to balance the transport and collection of separated charge carriers. This mechanism enables stable and reversible photocurrent polarity under illumination from opposite directions, reduces the minimum irradiance required for ambipolar operation from 175 mW cm^{-2} to 0.1 mW cm^{-2}. The resulting AEV array directly suppresses background-induced photocurrent offsets and exhibits bidirectional response times of ~20 μs, more than 10 times shorter than those of previously reported devices. It further achieves nearly 100% recognition accuracy under strong background illumination. These results establish a device-level strategy for rapid and reliable visual perception under optically challenging conditions.

2 | Results and Discussion

This ambipolar organic photodetector employs an optimized vertically stacked architecture. Its photoactive layer, comprising a P3HT:$PC_{71}BM$ bulk heterojunction (BHJ) (Figure 1a), features two critical design aspects: (i) substantially enhanced BHJ thickness (≈3 μm, conventional counterparts ~500 nm [21]); and (ii) symmetric PEDOT:PSS electrodes establishing practically identical Schottky barrier heights at both interfaces. The symmetric PEDOT:PSS electrodes, possessing a high work function (~5.0 eV; Figures S1 and S2), induce electric fields of comparable magnitude ($|E_1| \approx |E_2|$) but opposite polarity at both interfaces, resulting in a near-zero net built-in electric field (E_{net}) across the device.

$$E_{net} = \frac{\Delta\Phi_{top} - \Delta\Phi_{bottom}}{e \cdot d} \approx 0 \quad (1)$$

Under this condition, carrier transport becomes diffusion-dominated, exhibiting pronounced spatial dependence on photon absorption position. Optical/electrical simulations (Figure 1b) demonstrate that carrier generation occurs within a ~300 nm from the corresponding irradiated side of the P3HT:$PC_{71}BM$ heterojunction. Here, photogenerated electron-hole pairs undergo rapid dissociation at phase interfaces. Crucially, illumination geometry determines the collection pathway: top and bottom illumination generate different carrier distributions in the thick BHJ, leading to position-dependent collection pathways and opposite photocurrent polarities.

Current–voltage (*I*–*V*) characterization under dark conditions and illumination (top/bottom incidence) reveals three distinct optoelectronic properties defined by applied bias voltage (Figure 1c and Table S1): an ambipolar regime (−4 mV < *V* < 6 mV), a negative-response regime (−35 mV < *V* < −5 and 6 mV < *V* < 60 mV), and a unipolar regime (*V* < −35 mV and *V* > 60 mV). Note that precise transition voltages may vary slightly between devices. Steady-state photoswitching measurements further highlight divergent photocurrent dynamics across these bias ranges (Figure 1d–f), characterized as follows: (I) ambipolar regime (Figure 1d): Illumination of either the top or bottom electrode enhances the photocurrent over dark-state levels. Crucially, the photocurrent polarity reverses with illumination side, yielding positive or negative responses for top- or bottom-side illumination, respectively. (II) Negative-response regime (Figure 1e): Illumination reduces the net current magnitude below dark-state levels, constituting a negative photocurrent response. (III) Unipolar regime (Figure 1f): Illumination enhances the photocurrent significantly relative to dark-state levels. Crucially, the current flow direction remains invariant that determined solely by the applied bias polarity while light intensity modulates only its amplitude. Systematic characterization of the device's optoelectronic properties under ambipolar operation mode reveals a consistent and polarity-switchable response across the 300–600 nm spectral range (Figures 1g, S3, and S4), together with the measured noise-current spectral density and corresponding frequency-dependent specific detectivity (Figure S5). Specifically, top illumination generates a positive photocurrent ($I_{ph,\,top} > 0$), whereas the bottom illumination yields a negative photocurrent ($I_{ph,\,bottom} < 0$), confirming the bidirectional photoresponse modulation.

15214095, 0, Downloaded from https://advanced.onlinelibrary.wiley.com/doi/10.1002/adma.75139 by Fudan University, Wiley Online Library on [04/10/2026]. See the Terms and Conditions (https://onlinelibrary.wiley.com/terms-and-conditions) on Wiley Online Library for rules of use; OA articles are governed by the applicable Creative Commons License

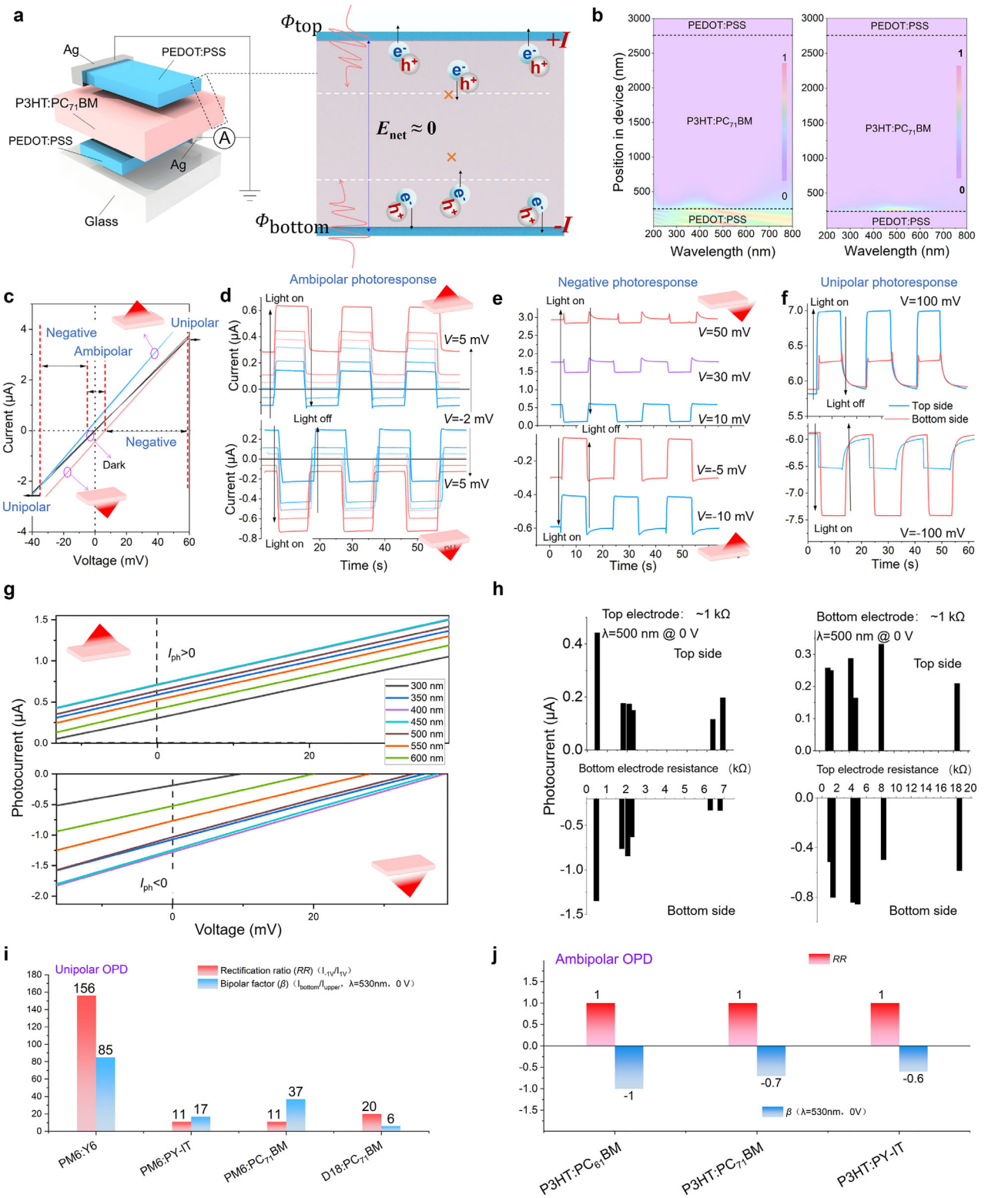

FIGURE 1 | Ambipolar photodiode: design, working mechanism, and operational characteristics. (a) Schematic of the ambipolar device structure and illustration of carrier transport under top and bottom illumination. (b) Spectrally and spatially resolved optical-field intensity (left) and photocarrier-generation (right) distributions (structure: glass/PEDOT:PSS/P3HT:$PC_{71}BM$/PEDOT:PSS). (c) Representative current–voltage (*I–V*) characteristics of operational voltage ranges for ambipolar-response, negative-response, and unipolar-response regions. (d) Typical current–time (*I–t*) response of ambipolar operation. (e) Typical *I–t* response of negative response. (f) Typical *I–t* response of unipolar operation. (g) Photocurrent–voltage curves under top and bottom illumination with varying illumination wavelengths. (h) Output photocurrents under top and bottom illumination while adjusting the top and bottom electrode resistance. Rectification ratio (RR) and ambipolarity factor (β) of the device upon modification of the donor, acceptor, or both donor/acceptor in the photoactive layer (i) unipolar and (j) ambipolar photoresponse systems.

15214095, 0, Downloaded from https://advanced.onlinelibrary.wiley.com/doi/10.1002/adma.75139 by Fudan University, Wiley Online Library on [04/10/2026]. See the Terms and Conditions (https://onlinelibrary.wiley.com/terms-and-conditions) on Wiley Online Library for rules of use; OA articles are governed by the applicable Creative Commons License

It is noteworthy that this ambipolar photoresponse demonstrates high robustness to variations in top/bottom electrode series resistances (0.5–180 kΩ range, Figures 1h and S6; Table S2). When fixing the bottom-electrode resistance at 1 kΩ, photocurrent intensity progressively decreases with lower top-electrode resistance; conversely, the photocurrent amplitude exhibits a weaker correlation to the bottom-electrode variations as top-electrode resistance fixed (1 kΩ). Nevertheless, photocurrent gain saturation initiates when top-electrode resistance falls below the 0.5 kΩ. At ultralow resistances (<0.1 kΩ), a dark current surge emerges that ultimately overwhelms the positive photocurrent signal in the top side, allowing detection of only a dominant negative photocurrent in the bottom side (Figure S7). These results also show that the front/back responsivity ratio can be tuned by electrode resistance, providing a structural route to adapt the device to calibrated or anisotropic background illumination (Figure S8).

To investigate the dependence of this effect on device parameters, we systematically modulated key parameters includes photosensitive layer thickness (d = 200 nm–5 μm; Figure S9 and Table S3), electrode work function (Figures S10–S13 and Table S4) and P3HT baches (Figure S14). The ambipolarity factor is defined as β: $\beta = \frac{I_{ph,\,bottom}}{I_{ph,\,top}}$, here, $\beta > 0$ indicates unipolar behavior, while $\beta < 0$ signifies the ambipolar state. At a thickness d = 3 μm and the electrode work function was tuned to approximately 5.0 eV, optimized ambipolar photoresponse under zero bias (@0 V) was achieved. To assess this ambipolar architecture's material dependence and transferability, we characterized seven representative donor–acceptor systems across three categories (Table S5): co-varied donor/acceptor components (e.g. PM6:Y6, Figure S15a,b); fixed-acceptor ($PC_{71}BM$) with varied donors (e.g. PM6:$PC_{71}BM$, Figure S15c,d); and fixed-donor (P3HT) with varied acceptors (e.g. P3HT:PY-IT, Figure S15e,f). Systems lacking P3HT exhibited strong unipolar characteristics ($\beta > 6$) (Figure 1i). Devices exhibiting the ambipolar photoresponse ($\beta < 0$) invariably contained a P3HT component (Figure 1j). The distinct behaviors indicate that polarity reversal requires not only structural symmetry but also balanced bulk transport and interfacial carrier collection, which are not achieved in the investigated PM6-based devices. These findings suggest P3HT-based systems as suitable model platforms for the present ambipolar architecture. The corresponding design principles, including weak net vertical built-in field, symmetric Schottky contacts, and diffusion-dominated transport, are summarized in Table S6.

Building upon these findings, we employed P3HT:$PC_{71}BM$ as a model bulk-heterojunction system to investigate the physical mechanism of illumination-direction-dependent ambipolar photoresponse in a thick vertical device architecture. Microscopic characterization revealed significant vertical phase segregation in P3HT:$PC_{71}BM$ heterojunction films. Atomic force microscopy (AFM) and scanning electron microscopy (SEM) analyses identified periodic micron-scale surface wrinkles (periodicity: ~5 μm; R_q: ~140 nm; Figure 2a). In contrast, the bottom surface of BHJ deposited on glass/PEDOT:PSS exhibited a smooth morphology (R_q: ~5 nm). Cross-sectional energy-dispersive x-ray spectroscopy (EDS) elemental mapping confirmed vertical phase separation, showing a gradual decrease in sulfur concentration (a P3HT indicator) from 11.55 wt% at the top surface to 3.41 wt% at the bottom (Figure S16). This spatial heterogeneity originates from differential segregation kinetics in the thick-film system (thickness: 3 μm), resulting in a P3HT-rich layer over a $PC_{71}BM$-rich layer.

We quantified organic heterojunction wrinkle morphology using aspect ratio (A_r), defined as root-mean-square roughness (R_q) normalized by wrinkle periodicity. To regulate crystallization kinetics, we employed solvent engineering. As shown in Figures 2b and S17, the use of high-boiling-point solvent 1,2-dichlorobenzene (DCB; b.p. 180°C) enabled slow room-temperature evaporation (25°C), promoting long-range-ordered P3HT crystallites that induced pronounced wrinkles, yielding (A_r = 0.027). Conversely, chloroform (CF; b.p. 61°C) accelerated evaporation and P3HT crystallinity process. Consequently, A_r decreased to 0.018 and 0.012 for DCB:CF ratios of 1:1 and 1:3 (v/v), respectively. All DCB-based mixtures retained micron-scale textures, whereas high-temperature annealing (130°C) or pure CF both enabled near-instantaneous solvent removal that reduced R_q to ~5 nm, yielding nano-scale smooth surfaces. Micron-scale wrinkles form during slow evaporation of thick P3HT:$PC_{71}BM$ films as P3HT preferentially segregates to the air–liquid interface due to its low surface energy and fast crystallization [41, 42]. This process dynamically excludes $PC_{71}BM$ to form a crystalline surface layer that constrains in-plane contraction. Accumulated stress triggers buckling, releasing energy as wrinkles, with thick films amplifying this effect through enhanced contraction freedom.

To establish the structure–property relationship between wrinkle extent (A_r) and photodiode ambipolarity, we systematically characterized devices whose photsensitive-BHJ fabricated under a controlled crystallization process (Figures 2c, S18, and S19). Devices with the smoothed BHJ demonstrated anomalous unipolar-to-ambipolar switching: unipolar operation ($\beta > 0$) at $P < 175$ mW cm^{-2} transitioned to ambipolar operation ($\beta < 0$) at $P \geq 175$ mW cm^{-2}. This phenomenon primarily arises from trap states formed by interfacial defects generated during rapid crystallization (Figure S20). Devices with the micron-scale texture reduces the threshold light intensity for ambipolar response from 175 mW cm^{-2} to 0.1 mW cm^{-2}, corresponding to an approximately 1750-fold reduction. Meanwhile, the positive/negative photocurrent ratio β approaches −1, confirming a more balanced and ideal ambipolar output (Figure 2d).

To quantify the power-dependent behavior of the ambipolar photoresponse, we analyzed the photocurrent (I_{ph}) using the power-law relation $I_{ph} \propto (P)^{\alpha}$ (Figure 2e) (~4–370 mW cm^{-2}). The device exhibits a slightly sublinear power-law photoresponse with α = 0.96. Strikingly, deliberate suppression of BHJ surface wrinkles through CF solvent blending markedly degraded power-law photoresponse. Samples with intermediate wrinkle morphology (DCB:CF = 1:1, A_r = 0.018) exhibited significantly lower α values (0.87 top/0.86 bottom), while low-wrinkle samples (DCB:CF = 1:3, A_r = 0.012) showed substantially greater degradation ($\alpha \approx 0.73$ top/0.85 bottom). This pronounced decline suggests that smoothed morphologies likely enhance carrier loss through increased bimolecular recombination. Furthermore, micron-scale corrugated devices maintained slightly sublinear power-law responses ($\alpha \approx 0.98$ top/0.95 bottom) at low irradiances (~0.1–1.7 mW cm^{-2}) (Figure S21), demonstrating robust ambipolar operation across a wide power range.

15214095, 0, Downloaded from https://advanced.onlinelibrary.wiley.com/doi/10.1002/adma.75139 by Fudan University, Wiley Online Library on [04/10/2026]. See the Terms and Conditions (https://onlinelibrary.wiley.com/terms-and-conditions) on Wiley Online Library for rules of use; OA articles are governed by the applicable Creative Commons License

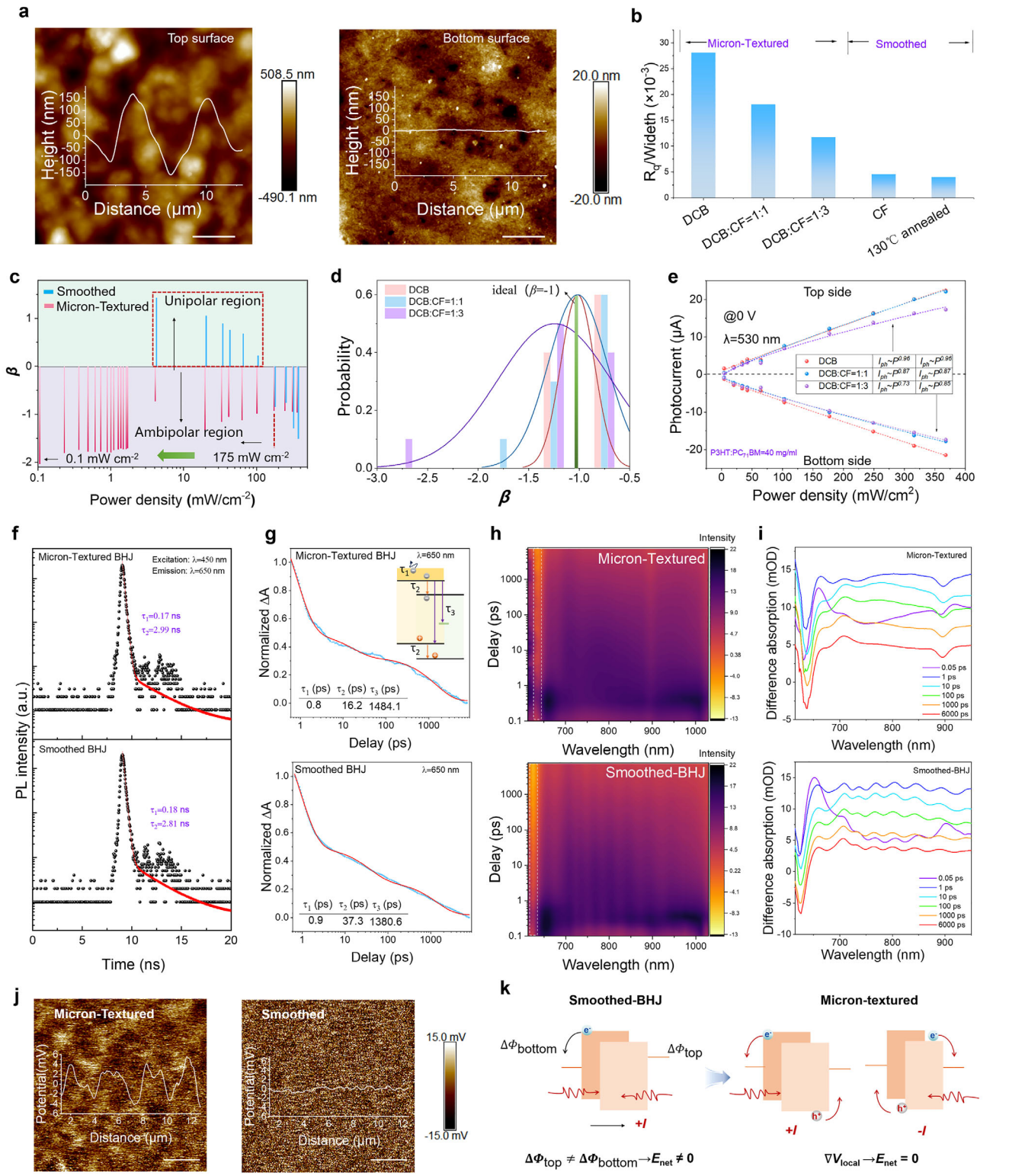

FIGURE 2 | Micro-textured photoactive layer: Morphology control, characterization, and charge transport dynamics. (a) Atomic force microscopy (AFM) height images of the top (left) and bottom (right) surfaces of the P3HT:$PC_{71}BM$ blend photoactive layer for the ambipolar device (scale bar: 4 μm). (b) Variation of film surface aspect ratio (A_r) for BHJ films regulated by solvent composition (DCB/CF ratio) and annealing temperature. (c) The ambipolarity factor β for devices based on micron-scale texture and smoothed BHJ films. (d) Distribution of the ambipolarity factor β regulated by surface wrinkle structures. (e) Photocurrent–power density (I_{ph}–P) dependence and exponential fitting curves for BHJ films with differing A_r. (f) Transient photoluminescence (TRPL) decay curves. (g) Normalized transient absorption (TA) decay traces monitored at 650 nm. (h) Wavelength-dependent TA kinetics: (i) Ensemble TA spectra at selected time delays. (j) Surface potential variation measured by Kelvin probe force microscopy (KPFM) of micron-textured (left) and smoothed (right) BHJ surfaces (scale bar: 4 μm). (k) Schematic illustration of carrier separation and transport at the smoothed (left) and micron-textured (right) interface under illumination below 175 mW cm^{-2}.

15214095, 0, Downloaded from https://advanced.onlinelibrary.wiley.com/doi/10.1002/adma.75139 by Fudan University, Wiley Online Library on [04/10/2026]. See the Terms and Conditions (https://onlinelibrary.wiley.com/terms-and-conditions) on Wiley Online Library for rules of use; OA articles are governed by the applicable Creative Commons License

To examine how wrinkle textures regulate carrier dynamics, carrier recombination in BHJ was studied using steady-state photoluminescence (PL) and time-resolved PL (TRPL) spectroscopy (Figures 2f and S22). Steady-state PL showed similar emission intensities in textured and smooth films, indicating no significant increase in non-radiative pathways. TRPL biexponential analysis revealed: The fast decay τ_1 (defect-assisted recombination) remained consistent across samples (0.17–0.18 ns; textured: 0.17 ns, smooth: 0.18 ns). The slow decay τ_2 (radiative recombination) increased by 6.4% in textured films (2.99 ns vs. smooth 2.81 ns). These results indicate that micron-scale textures do not induce extra defect-mediated recombination and may facilitate more effective or rapid charge transfer. The signals in the 10–15 ns range represent the charge transfer state recombination or trapped charge recombination in the P3HT:$PC_{71}BM$ blend [43, 44].

Further insights into the ultrafast dynamics of the BHJs were obtained through transient absorption spectroscopy (TAS). Triexponential fitting identified three distinct relaxation processes (Figure 2g). The initial relaxation time constant τ_1 (<1 ps) showed negligible variation with micron-scale wrinkle formation, indicating this ultrafast process is intrinsically governed by intramolecular excited-state relaxation. In notable contrast, the τ_2 relaxation time for micro-textured structures shortened to 16.2 ps (from 37.3 ps in smooth morphologies). This reflects enhanced exciton dissociation in micro-textured domains, where 650 nm absorption is mainly attributed to P3HT's electronic transition (Figure S23). The τ_3 relaxation time for micro-textured structures lengthened from 1380.6 ps to 1484.1 ps. The extended τ_3 lifetime demonstrates suppression of non-radiative recombination and bimolecular annihilation pathways by the micron-scale periodic topography. Additionally, a 14 nm redshift (625 → 639 nm, Figure 2h,i) was observed in the ground-state bleaching (GSB) signal. The oscillatory features in smoothed BHJ arise from specular interference between the smooth surface and substrate. The redshift in micro-textured BHJ may stems from texture-induced lattice distortions lowering exciton binding energies [45], consistent with the broadening of the in-plane (100) scattering peak observed in micron-textured BHJ, with an FWHM of 0.25 versus 0.22 in smoothed BHJ (Figure S24; Tables S7 and S8).

Surface wrinkles induce tensile strain at ridge crests and compressive strain in groove valleys, creating significant strain gradients [46]. These gradients can generate local polarization, causing spatial separation of bound charges and inducing a ≈10 mV localized potential gradient (Figure 2j). This periodic potential modulation may assist in balancing the transport and collection of already separated carriers, thereby stabilizing ambipolar photocurrent output (Figure 2k). This distinguishes the micro-textured BHJ from planar films, where carrier collection is more susceptible to the residual vertical built-in field caused by vertical composition gradients and imperfectly matched top/bottom interfacial barriers.

Ultrathin optoelectronic devices, characterized by lightweight construction [47] and micron-scale thickness (parylene 5 μm/PEDOT:PSS/P3HT:$PC_{71}BM$/PEDOT:PSS, ~8 μm total; Figure 3a), exhibit exceptional conformability to complex curved surfaces. Quantitative atomic force microscopy (Q-AFM) measurements revealed that micron-scale wrinkle formation redistributes strain energy, enhancing both the elastic modulus and surface adhesion force of the organic heterojunction as the wrinkle aspect ratio increases (Figures 3b and S25). The device demonstrates remarkable mechanical adaptability, conforming precisely to both structured geometries (e.g., 3-mm-diameter cylinders/conical tips) and anatomical contours (e.g., skin microstructures during joint articulation; Figure 3c). After 3500 bending cycles at a 3 mm diameter , the internal Schottky symmetry remains intact, and its photocurrent magnitude and ambipolar output were essentially preserved (Figure 3d). To evaluate endurance limits, we conducted accelerated bending fatigue testing (>10 000 cycles). Monitoring revealed ~93% and ~84% retention of initial top-illuminated photocurrent after 5000 and 10 000 cycles (Figure 3e,f), with performance degradation correlating with potential stress-induced delamination at the electrode–heterojunction interface (Figure S26). Figure 3g reveals a marginal photocurrent decrease over 70 bending cycles, which is attributed to hot-carrier-induced exciton annihilation under continuous illumination [48].

Leveraging the device's zero-bias ambipolar photocurrent properties, the array has potential to detect of faint optical signals against bright backgrounds by effectively suppressing background-induced photocurrent offset during abrupt dark-to-light transitions. This capability is functionally inspired by photonic adaptation in biological vision [49, 50]: the cone-rod regulatory cascade triggered by drastic illumination changes. As shown in Figure 4a,b, sudden exposure to intense background illumination (>10 mW cm^{-2}) initiates a physiological photoadaptation cascade: pupil constriction reduces light influx, cone cells dominate imaging, and rod cells decrease photosensitivity via rhodopsin bleaching [51]. While this process preserves vision, it incurs a seconds-long response delay.

Inspired by photoadaptive cascades, we developed an ultrathin, flexible, curved AEV array (Figure 4c). Unlike biological vision, which requires temporal adaptation, this system enables rapid background-offset suppression during abrupt background-illumination transitions, without perceptible delays (Figure 4d). The architecture enables in-sensor background-offset suppression for preprocessing: under an abrupt change in calibrated bifacial background illumination, positive background photocurrent (I_{B1}) is partially compensated by concurrent negative photocurrent (I_{B2}) at the bottom interface. This reduces the residual background-induced offset under calibrated bifacial background illumination. This AEV mechanism constitutes a device-level strategy that enables direction-dependent (positive/negative) photocurrent generation within a single pixel at near-zero bias. Such intrinsic ambipolarity enables pixel-level background-offset suppression directly at the photodetection interface, achieving a functional photonic-adaptation time of ~20 μs, which is shorter than those of previously reported artificial vision systems [52], and >1000 times faster than the human eye (Figure 4e) [51]. Transient photoresponse measurements under 532 nm excitation reveal ultrafast rise and decay times (τ_r, τ_d): specifically, 20.0 μs/11.7 μs for top illumination and 13.1 μs/17.1 μs for bottom illumination (Figure 4f,g).

Leveraging its inherent ambipolar photoresponse, the AEV device enables optical subtraction under intense ambient light, thereby effectively suppressing background-induced photocurrent offset. As illustrated in Figure 4h, increasing the background

15214095, 0, Downloaded from https://advanced.onlinelibrary.wiley.com/doi/10.1002/adma.75139 by Fudan University, Wiley Online Library on [04/10/2026]. See the Terms and Conditions (https://onlinelibrary.wiley.com/terms-and-conditions) on Wiley Online Library for rules of use; OA articles are governed by the applicable Creative Commons License

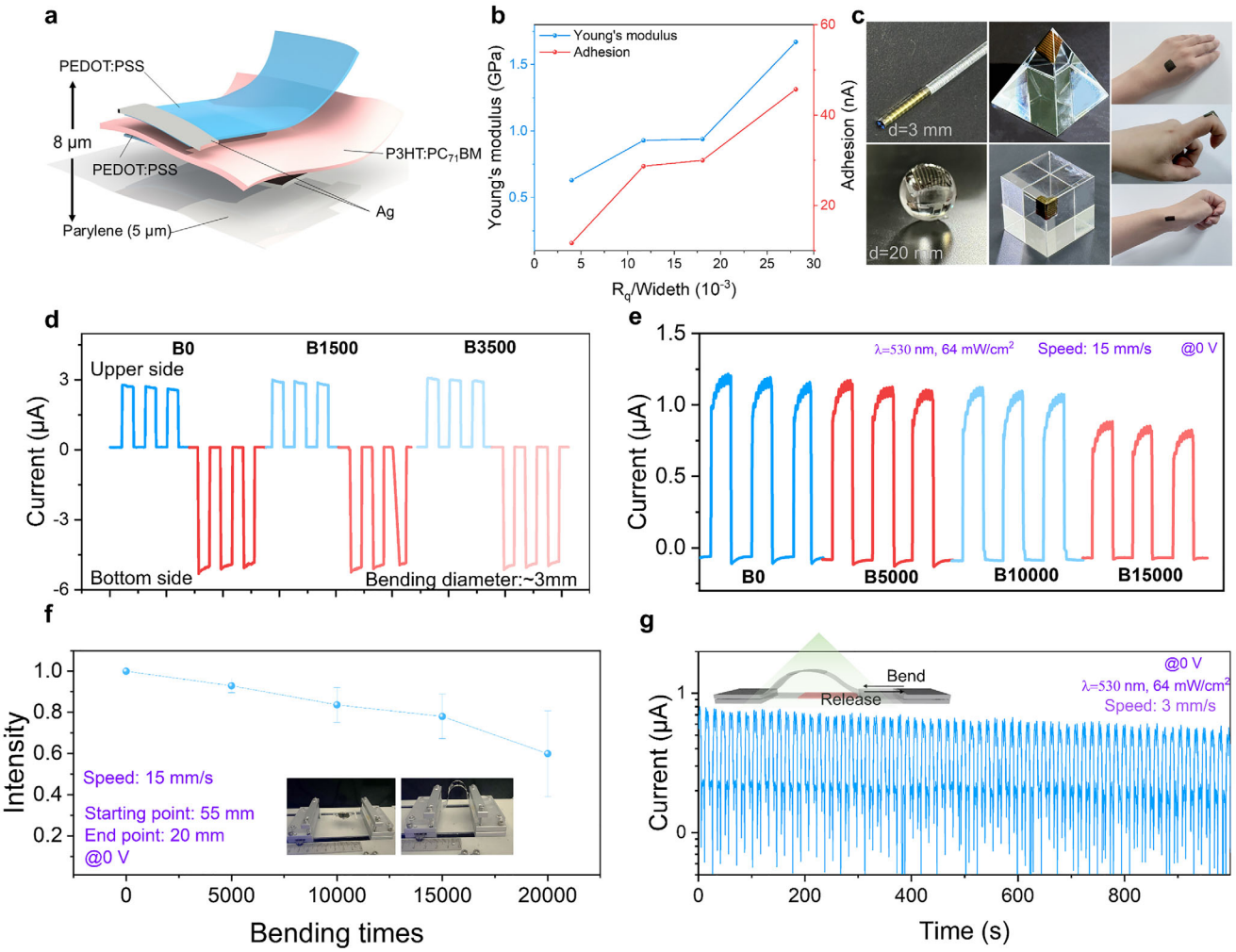

FIGURE 3 | Ultra-flexible ambipolar devices: Conformal integration and mechanical endurance. (a) Schematic of the ultra-thin flexible ambipolar device architecture: parylene/PEDOT:PSS/P3HT:$PC_{71}BM$/PEDOT:PSS with a total thickness of ~8 μm. (b) Measured Young's modulus and adhesion force for BHJ films exhibiting different A_r. (c) Demonstration of conformal integration of ultra-thin devices onto geometrically diverse surfaces (cylinder, sphere, prism, pyramid, and curved skin). (d) Ambipolar photoresponse of device (bending diameter ~3 mm) after 0, 1500, and 3500 bending cycles. (e) *I–t* output from the top electrode under illumination during bending fatigue testing after 0, 5 000, 10 000, and 15 000 cycles. (f) Evolution of normalized photocurrent over 20 000 bending cycles. (g) Current output under simultaneous continuous illumination and bending stress.

intensity from 0 mW/cm^2 to 33 mW/cm^2 shifts the baseline current from ~0.08 μA to ~−0.12 μA. Conversely, the signal-induced photocurrent decreases only modestly, from 0.2 μA to 0.15 μA under the same conditions. At a fixed background of 11 mW cm^{-2} (Figure 4i), the device maintained distinguishable light/dark switching signals even at a signal light intensity of only 0.4 mW cm^{-2}, which was a mere ~4% of the background intensity.

To quantitatively evaluate the dim-light recognition capability of the AEV pixel during abrupt background-illumination transitions. The SNR of the photodetector is expressed as [30, 53],

$$\mathrm{SNR} = \frac{n_{es}}{\bar{n}_{en}} = \frac{I_s}{\left(\overline{I_N^2}\right)^{1/2}} \tag{2}$$

where, n_{es} represent the number of photoelectrons generated for the target signal, while n_{en} is the root mean square of the equivalent photoelectron amount of the total noise. I_s represents signal current, I_N is the sum of noise currents, including shot noise, transfer noise, and thermal noise. Under intense ambient illumination, background-current noise dominates, and Equation (2) can be simplified as:

$$SNR_{eff} = \frac{I_s}{\left(\overline{I_B^2}\right)^{\frac{1}{2}}} \tag{3}$$

During the transition from dark to bright environments (Figure 4j,k), the SNR of the ambipolar device remained relatively stable. This indicates that the environmental shift caused only a moderate SNR decline with dim-light signal recognition (1 mW cm^{-2}). Consistent with this behavior, under low-signal conditions (0.3 mW cm^{-2}), the ambipolar device exhibited negligible interference (Figure 4k). Conversely, the unipolar electronic vision (UEV) device—implemented using unilateral mixed-light illumination simulations—primarily

15214095, 0, Downloaded from https://advanced.onlinelibrary.wiley.com/doi/10.1002/adma.75139 by Fudan University, Wiley Online Library on [04/10/2026]. See the Terms and Conditions (https://onlinelibrary.wiley.com/terms-and-conditions) on Wiley Online Library for rules of use; OA articles are governed by the applicable Creative Commons License

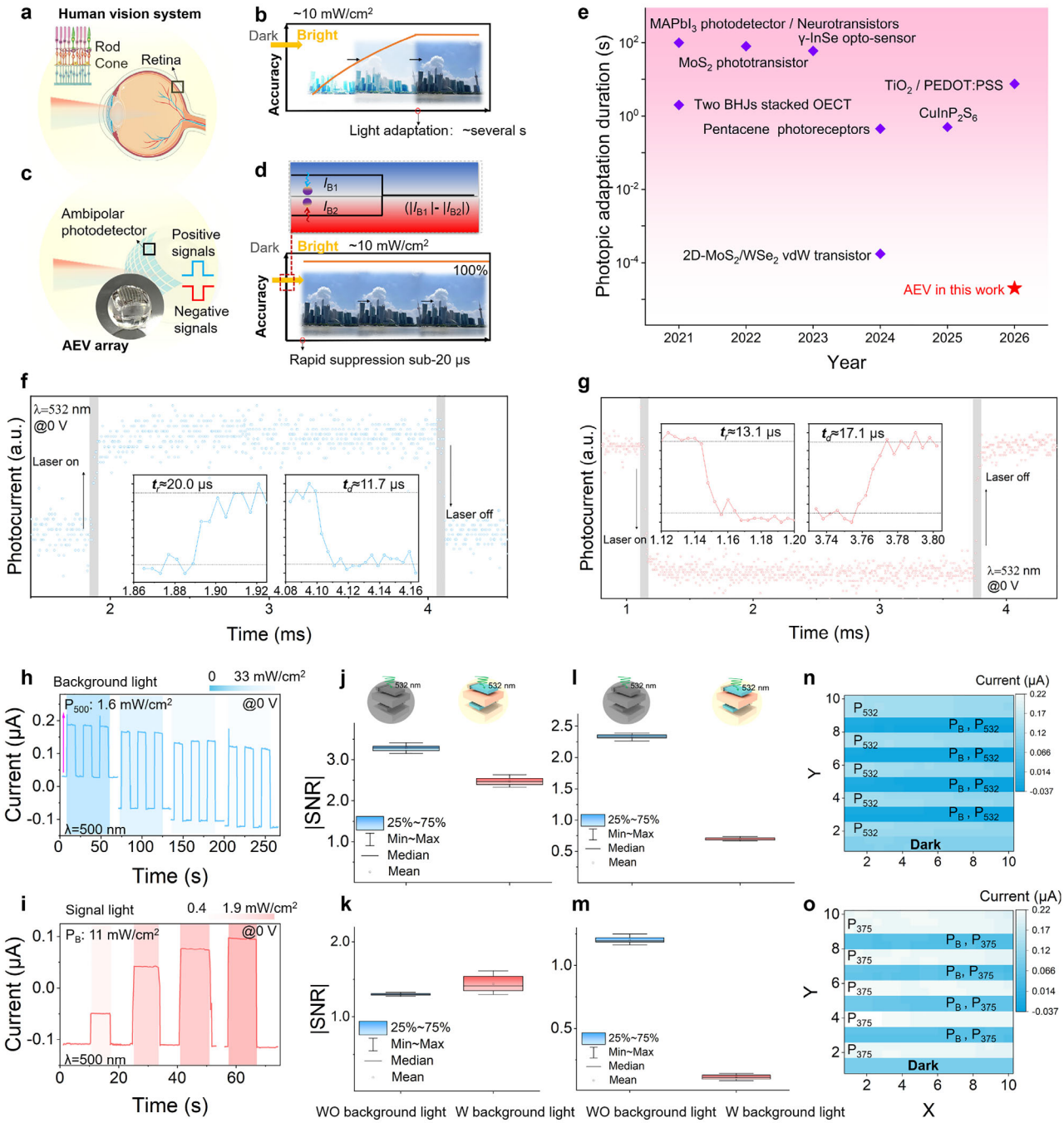

FIGURE 4 | Bio-inspired AEV: Mechanism and background-suppression capability. (a) Schematic of the human vision system. (b) Slow adaptation process of human vision transitioning from a dark to a bright environment. (c) Structural schematic of the bio-inspired dual-side-sensitive AEV array. (d) Rapid suppression of background-light-induced noise by the AEV array upon transitioning from dark to bright illumination; illustration: Background light suppression mechanism: Ambient light incident from the device top generates photocurrent (I_{B1}), while light incident from the bottom generates the complementary photocurrent (I_{B2}), resulting in effective background cancellation (net current ≈ I_{B1}–I_{B2}) for omnidirectional background illumination. (e) Comparison of the functional photoadaptation times of representative artificial vision systems. The values represent characteristic timescales for adaptive responses in the reported systems [6, 51, 52, 54–60]. (f and g) Transient photoresponse times of the AEV pixel measured under top-illumination (f) and bottom-illumination (g) at 0 V. (h) *I*–*t* response of the AEV device under a fixed weak signal light power (1 mW cm^{-2}) and varying background light power (0–33 mW cm^{-2}). (i) *I*–*t* response of the AEV device under a fixed background light power (11 mW cm^{-2}) and varying signal light power (0.4–1.9 mW cm^{-2}). (j and k) Measured SNRs for the AEV pixel: I_{532}/I_d and I_{532+B}/I_B at signal light powers of (j) 1 mW cm^{-2} and (k) 0.3 mW cm^{-2} (background light at 11 mW cm^{-2}). (l and m) Measured effective SNRs (I_{532}/I_d and I_{532+B}/I_B) for a unipolar electronic vision (UEV) pixel at signal light powers of (l) 1 mW cm^{-2} and (m) 0.3 mW cm^{-2} (background light at 5 mW cm^{-2}). (n and o) Current mapping of the AEV pixel under continuous on-off switching of omnidirectional background illumination (11 mW cm^{-2}). (n) Current mapping under dynamic 532 nm signal light illumination (0.3 mW cm^{-2}) superimposed on switched background. (o) Current mapping under dynamic 375 nm signal light illumination (0.3 mW cm^{-2}) superimposed on switched background.

15214095, 0, Downloaded from https://advanced.onlinelibrary.wiley.com/doi/10.1002/adma.75139 by Fudan University, Wiley Online Library on [04/10/2026]. See the Terms and Conditions (https://onlinelibrary.wiley.com/terms-and-conditions) on Wiley Online Library for rules of use; OA articles are governed by the applicable Creative Commons License

generated positive photoelectric signals accompanied by the substantial background noise. Under equivalent conditions (Figure 4l,m), the SNR of UEV device decreased sharply from 2.2 to 0.6 and from 1.2 to 0.1. These results demonstrate that background light significantly hinders the unipolar device's recognition capability. The stability of the AEV pixel under dynamic brightness transitions was specifically evaluated. As shown in Figures 4n,o and S27, during the repeated dim-to-bright and bright-to-dim background switching cycles, the AEV device maintained distinguishable weak-signal responses from the strong-background state.

We fabricated an image sensor based on a 10 × 10 array of ambipolar photodiodes. To ensure electrode continuity and optical transparency, a 5 nm-thick gold (Au) electrode layer was deposited onto the array (Figure 5a), while the ambipolar device architecture enables background-offset suppression during abrupt light-to-dark transitions (Figure 5b). Photocurrent measurements confirmed all 100-pixel units functioned correctly, generating well-defined photocurrent response signals (Figure 5c).

To evaluate the imaging performance for weak target signals, we systematically compared the AEV array with UEV devices under the influence of strong background light interference. We further demonstrated the AEV array's capability for target pattern imaging under diverse conditions. By varying the signal light wavelength (530 and 365 nm; Figure 5d) and power (0.4–2 mW cm^{-2}; Figure 5e), this AEV array consistently produced clear images of the letters of 'T', 'H', 'J', and 'L'. Image clarity significantly improved with increasing signal light power. In contrast, under identical conditions, images from UEV devices were overwhelmed by intense background light noise, rendering the letter 'T' completely indistinguishable (Figure S28), highlighting the improved background-interference tolerance of the AEV array.

Conventional image sensors and the human retina require prolonged adaptation to abrupt intense illumination, temporarily impairing visual perception and posing safety risks (Figure 5f). In contrast, the AEV array suppresses background-induced photocurrent offsets at the photodetection interface, enabling real-time preprocessing while reducing downstream computational demands. To evaluate image recognition under strong ambient light, we integrated the AEV array with a multilayer convolutional neural network (CNN). The array suppresses background offsets and extracts weak target signals before CNN recognition (Figure 5g,h). In experiments, the AEV array was subjected to strong ambient background light (11 mW cm^{-2}). Five distinct traffic sign patterns ($\lambda = 530$ nm, intensities: 0.4 and 1 mW cm^{-2}) served as target signal sources, and a total of 10 test image data sets were acquired (Figures 5g and S29). Feeding these imaging signals into the pre-trained CNN for recognition yielded near-perfect validation accuracy (approaching 100%) after only eight training epochs (Figure 5h,i). To verify system generality, we tested it using four different letter patterns as targets, adjusting their wavelengths and power densities. The system consistently maintained a high recognition accuracy of approximately 85% (Figure S30a). As a control, the recognition accuracy of a system based on UEV devices, evaluated under identical strong background illumination, was severely degraded to only ~30% due to background-induced electrical noise interference (Figure S30b), significantly lower than that of the AEV-based system.

3 | Conclusions

In summary, combining nearly symmetric back-to-back Schottky contacts with a self-assembled, donor-enriched micron-textured photoactive layer enables illumination-direction-dependent photocurrent polarity control. The symmetric architecture minimizes the net vertical built-in field, while the textured surface introduces a localized potential variation (~10 mV) that may assist carrier transport and collection, thereby stabilizing the ambipolar photoresponse. This design reduces the minimum irradiance required for ambipolar operation from 175 mW cm^{-2} to 0.1 mW cm^{-2}, a 1750-fold reduction, and enables voltage-selectable ambipolar, negative, and unipolar response regimes. Based on this mechanism, an ~8 μm-thick flexible AEV array suppresses background-induced photocurrent offsets directly at the photodetection interface, achieving bidirectional response times of ~20 μs and nearly 100% recognition accuracy under strong background illumination. These results demonstrate a device-level approach to rapid and reliable visual perception in flexible electronic vision systems under intense ambient light.

4 | Materials and Methods

4.1 | Fabrication of Ambipolar and Unipolar OPD

Devices were fabricated on glass substrates. Glass substrates were cleaned sequentially with soapy water, deionized water, and ethanol, followed by a 5-min plasma treatment to enhance surface wettability. Prior to use, the PEDOT:PSS solution was diluted with ethanol to lower the mixture's melting point. The pretreated substrates were placed on a hotplate at approximately 130°C. The diluted PEDOT:PSS solution was then uniformly sprayed onto the heated substrates using a mask template to define the pattern and form the bottom electrode layer, with a thickness of approximately 300 nm.

Next, the samples were transferred into an argon-filled glovebox. The photoactive layer solution was prepared by dissolving P3HT and $PC_{71}BM$ in a 1:1 weight ratio (total concentration: 10, 20, 40, and 80 mg/mL) in a blended solvent of chloroform (CF) and *o*-dichlorobenzene (DCB) with varying ratios. This solution was stirred thoroughly at 70°C overnight on a hotplate. For samples with different photoactive layers (PM6:Y6, PM6:PY-IT, PM6:$PC_{71}BM$, D18:$PC_{71}BM$, P3HT:$PC_{61}BM$, P3HT:PY-IT), the donor:acceptor weight ratio was maintained at 1:1 with a total concentration of 40 mg/mL. Subsequently, the photoactive solution (~25 μL) was deposited onto the glass/PEDOT:PSS substrates at room temperature. The films were allowed to dry slowly to ensure complete solvent removal, followed by baking on a hotplate at 130°C for 30 min. For the rapid thermal annealing samples, annealing at 130°C was performed immediately after the precursor solution was deposited onto the glass/PEDOT:PSS substrates. Following the deposition of the photoactive layer, the samples were conducted with 30-s plasma treatment then transferred to a hotplate in ambient air. The diluted PEDOT:PSS solution was again uniformly sprayed to form the top electrode

15214095, 0, Downloaded from https://advanced.onlinelibrary.wiley.com/doi/10.1002/adma.75139 by Fudan University, Wiley Online Library on [04/10/2026]. See the Terms and Conditions (https://onlinelibrary.wiley.com/terms-and-conditions) on Wiley Online Library for rules of use; OA articles are governed by the applicable Creative Commons License

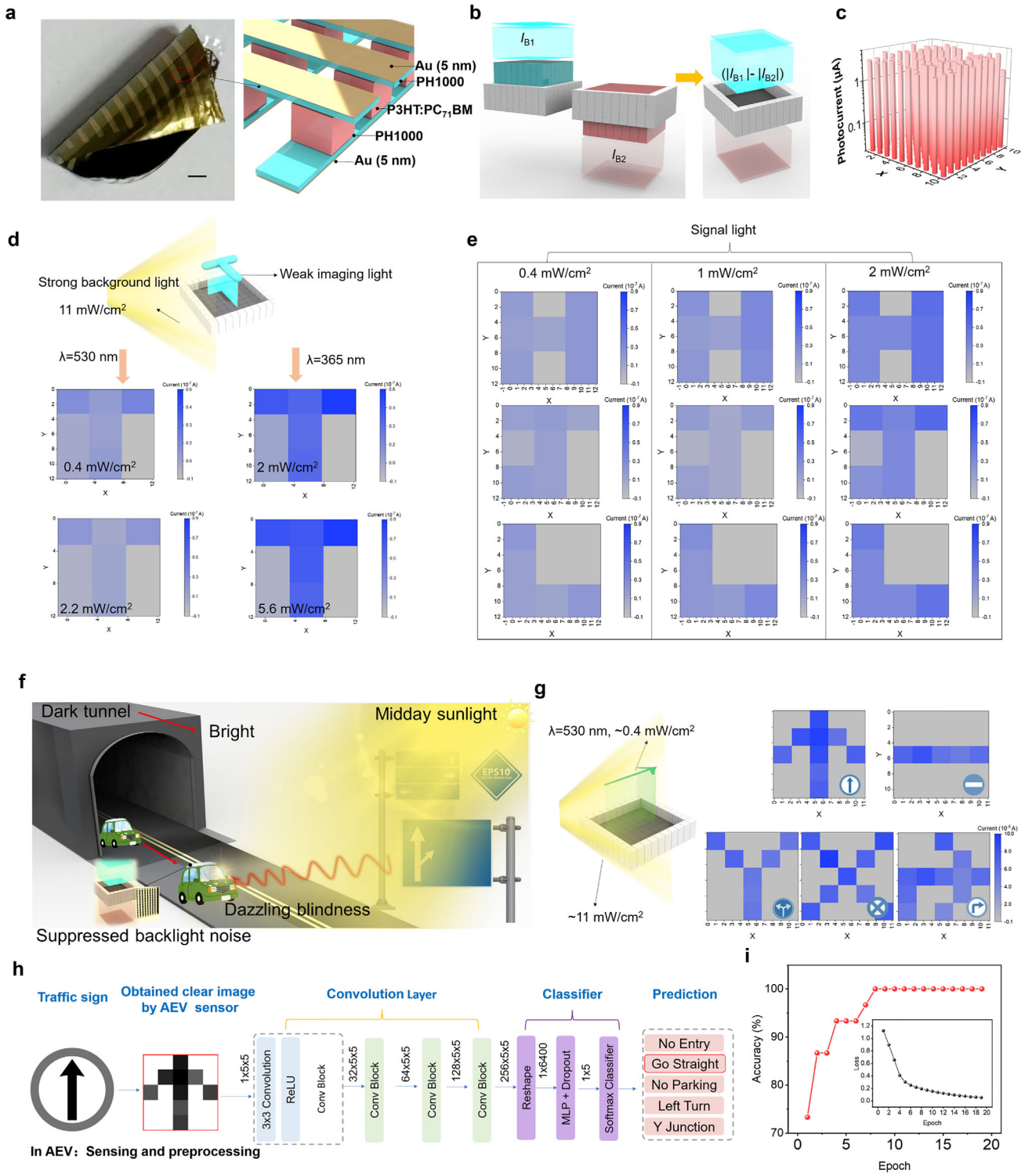

FIGURE 5 | Characterization and application of the AEV array sensor. (a) Optical micrograph (left) (scale bar: 5 mm) and schematic diagram (right) of the 10 × 10 AEV array. (b) Schematic of background-offset suppression in the AEV array and (c) distribution of photocurrent in the upper array region under mixed-wavelength illumination (total intensity: 5 mW cm^{-2}). (d) Imaging results of UV and visible signal sources under intense ambient background illumination (11 mW cm^{-2}). (e) Signal-dependent image responses at varying signal intensities (0.4, 1, and 2 mW cm^{-2}) with fixed background illumination (11 mW cm^{-2}). (f) Simulation of a vehicle transition from a dark tunnel to bright noon sunlight. (g) Traffic sign detection using AEV sensors under equivalent high-glare conditions, the images were reconstructed from experimentally measured pixel-current maps. (h) Machine learning workflow for traffic sign recognition: Current maps are processed through four convolutional blocks (each: 3 × 3 Conv → ReLU → 1 × 1 Pooling) followed by an MLP classifier (6400 × 128 → Dropout (0.5) → 128 × 5); (i) CNN-calculated recognition accuracy with corresponding loss function (inset).

15214095, 0, Downloaded from https://advanced.onlinelibrary.wiley.com/doi/10.1002/adma.75139 by Fudan University, Wiley Online Library on [04/10/2026]. See the Terms and Conditions (https://onlinelibrary.wiley.com/terms-and-conditions) on Wiley Online Library for rules of use; OA articles are governed by the applicable Creative Commons License

layer, approximately 300 nm thick, using a mask template oriented perpendicularly to the bottom electrode pattern.

4.2 | Fabrication of the AEV Array

The preparation of the AEV array was performed on a 5-μm-thick parylene substrate. The parylene thin film was meticulously deposited on a rigid glass substrate via vapor deposition techniques. Following the aforementioned steps, the PEDOT:PSS bottom electrode layer, P3HT:$PC_{71}BM$ photosensitive layer, and PEDOT:PSS top electrode layer were sequentially prepared. The difference is the use of a 10-column hollowed-out template to create a 10 × 10 array, where the overlap of the top and bottom electrodes constitutes individual pixels, each measuring 1 × 1 mm^2. Additionally, a 5-nm layer of gold (Au) was deposited on the bottom of the bottom electrode and the top of the top electrode to ensure the continuity of the array electrode via vacuum thermal evaporation. To facilitate subsequent testing, Ag is evaporated at the edges of the electrodes to serve as leads.

4.3 | Materials and Device Characterization

All solvents were purchased from Sinopharm China. Poly(3,4-ethylenedioxythiophene):poly(styrenesulfonate) [22] (PEDOT:PSS, Clevios PH1000) were purchased from Heraeus Inc., Germany. Poly(3-hexylthiphene) [61] (P3HT) and [6,6]-phenylC71 butyrate methyl ester [62] ($PC_{71}BM$) were purchased from Advanced Election Technology Co., Ltd. Photophysical properties were characterized via steady-state/transient PL spectroscopy (Edinburgh FLS1000, UK) and fs-TAS (Ultrafast Systems Helios, US); morphological/electronic structures were probed by atomic force microscopy operating in Q-mode, KPFM, and tapping-mode (Bruker Dimension Icon) with complementary SEM (Hitachi SU8010).

The optoelectronic parameters of photodetectors were investigated by Keithley 4200 with the light source system consisting of an Xe lamp (HORIBA, 450 W) and a monochromator, whose wavelength can be tuned from UV (~250 nm) to visible light (~700 nm). The response time test is conducted using a system comprised of a chopper-controlled laser (532 nm) and an oscilloscope (Tektronix MSO/DPO5000). The optical field distribution of OPD was simulated by optical admittance analysis and the wavelength-dependent, and refractive index (n) and extinction coefficients (k) of photosensitive layer were measured by the dual rotating-compensator Mueller matrix ellipsometer (ME-L ellipsometer, Wuhan Eoptics Technology Co.). All device characterizations were conducted in ambient air.

4.4 | Simulation of Neural Network Classifier

We employed a CNN-based system as a classifier to evaluate the efficiency of image recognition under strong ambient illumination. Specifically, the system was designed to classify images processed by a AEV image sensor. To train the deep learning model, a substantial dataset was required. Considering the high cost of acquiring real-world datasets, we generated synthetic images automatically for training and validation, while reserving an experimental dataset for testing. The synthetic images were generated with varying shades based on the shape characteristics of different objects. Additionally, data augmentation techniques, including rotations (90°, 180°, and 270°) and vertical mirroring, were applied to enhance the diversity of the dataset. As a result, we constructed a dataset comprising 6000 images, with 5400 used for training and the remaining 600 for validation.

We then designed a four-layer convolutional neural network to learn the patterns inherent in these images. Each convolutional block consisted of a 3 × 3 convolutional kernel (padding = 1, stride = 1), followed by a ReLU activation layer. Through these four convolutional layers, with channel sizes of 32, 64, 128, and 256, respectively, the original input images of size 5 × 5 were transformed into 256 × 5 × 5 feature tensors. These tensors were subsequently reshaped and passed through multilayer perceptrons to reduce the dimensionality to 1 × 5 vectors. Finally, a softmax layer was used to assign probabilities to each predefined label, enabling image classification.

For optimization, we employed the Adam [63] optimizer with a learning rate of 1×10^{-5} to minimize the loss function during training. During the testing phase, the trained model was used to predict the labels of real images acquired from AEV sensors. Accuracy was chosen as the evaluation metric to assess model performance. The entire model was implemented using the PyTorch [64] framework on an Ubuntu 20.04 system.

Author Contributions

Tingting Yan: data curation, formal analysis, investigation, writing – original draft, methodology. **Yarong Gu**: data curation, formal analysis, writing – review and editing. **Bobo Li**: formal analysis, software, writing – review and editing. **Ming Deng**: data curation, formal analysis, writing – review and editing. **Zijin Zhao**: data curation, formal analysis, writing – review and editing. **Ziqing Li**: data curation, formal analysis, writing – review and editing. **Junhao Chu**: supervision. **Limin Wu**: conceptualization, writing – review and editing, supervision. **Xiaosheng Fang**: conceptualization, investigation, data curation, supervision, writing – review and editing.

Acknowledgements

This work was sponsored by the National Natural Science Foundation of China (Grant Nos. 52425308, 62374035, 92263106, and 52502168) and the Shanghai Sailing Program (No. 24YF2701800).

Conflicts of Interest

The authors declare no conflicts of interest.

Data Availability Statement

The data that support the findings of this study are available in the Supporting Information of this article.

References

1. G. Marriott, S. Mao, T. Sakata, et al., "Optical Lock-In Detection Imaging Microscopy for Contrast-Enhanced Imaging in Living Cells," *Proceedings of the National Academy of Sciences* 105 (2008): 17789–17794, http://www.jstor.org/stable/25465362.

15214095, 0, Downloaded from https://advanced.onlinelibrary.wiley.com/doi/10.1002/adma.75139 by Fudan University, Wiley Online Library on [04/10/2026]. See the Terms and Conditions (https://onlinelibrary.wiley.com/terms-and-conditions) on Wiley Online Library for rules of use; OA articles are governed by the applicable Creative Commons License

2. J. W. Zhang, M. Zhuang, B. Wang, et al., "Entanglement-Enhanced Quantum Lock-In Detection Achieving Heisenberg Scaling," *Nature Communications* 17 (2026): 149, https://doi.org/10.1038/s41467-025-66828-z.

3. T. Jiang, Y. Wang, W. Huang, et al., "Retina-Inspired Organic Neuromorphic Vision Sensor With Polarity Modulation for Decoding Light Information," *Light: Science & Applications* 12 (2023): 264, https://doi.org/10.1038/s41377-023-01310-3.

4. C. Jo, J. Kim, J. Y. Kwak, et al., "Retina-Inspired Color-Cognitive Learning via Chromatically Controllable Mixed Quantum Dot Synaptic Transistor Arrays," *Advanced Materials* 34 (2022): 2108979, https://doi.org/10.1002/adma.202108979.

5. D. Kumar, L. Joharji, H. Li, A. Rezk, A. Nayfeh, and N. El-Atab, "Artificial Visual Perception Neural System Using a Solution-Processable MoS_2-Based In-Memory Light Sensor," *Light: Science & Applications* 12 (2023): 109, https://doi.org/10.1038/s41377-023-01166-7.

6. F. Liao, Z. Zhou, B. J. Kim, et al., "Bioinspired In-Sensor Visual Adaptation for Accurate Perception," *Nature Electronics* 5 (2022): 84–91, https://doi.org/10.1038/s41928-022-00713-1.

7. Y. Tan, H. Hao, Y. Chen, et al., "A Bioinspired Retinomorphic Device for Spontaneous Chromatic Adaptation," *Advanced Materials* 34 (2022): 2206816, https://doi.org/10.1002/adma.202206816.

8. P. Xie, Y. Xu, J. Wang, et al., "Birdlike Broadband Neuromorphic Visual Sensor Arrays for Fusion Imaging," *Nature Communications* 15 (2024): 8298, https://doi.org/10.1038/s41467-024-52563-4.

9. K. Chen, H. Hu, I. Song, et al., "Organic Optoelectronic Synapse Based on Photon-Modulated Electrochemical Doping," *Nature Photonics* 17 (2023): 629–637, https://doi.org/10.1038/s41566-023-01232-x.

10. D. Wang, X. Liu, Y. Kang, et al., "Bidirectional Photocurrent in p–n Heterojunction Nanowires," *Nature Electronics* 4 (2021): 645–652, https://doi.org/10.1038/s41928-021-00640-7.

11. T. Yan, Z. Li, F. Cao, J. Chen, L. Wu, and X. Fang, "An All-Organic Self-Powered Photodetector With Ultraflexible Dual-Polarity Output for Biosignal Detection," *Advanced Materials* 34 (2022): 2201303, https://doi.org/10.1002/adma.202201303.

12. F. Zhou and Y. Chai, "Near-Sensor and In-Sensor Computing," *Nature Electronics* 3 (2020): 664–671, https://doi.org/10.1038/s41928-020-00501-9.

13. X. Zhu, C. Gao, Y. Ren, et al., "High-Contrast Bidirectional Optoelectronic Synapses Based on 2D Molecular Crystal Heterojunctions for Motion Detection," *Advanced Materials* 35 (2023): 2301468, https://doi.org/10.1002/adma.202301468.

14. W. Cheng, S. Wu, J. Lu, et al., "Self-Powered Wide-Narrow Bandgap-Laminated Perovskite Photodetector With Bipolar Photoresponse for Secure Optical Communication," *Advanced Materials* 36 (2024): 2307534, https://doi.org/10.1002/adma.202307534.

15. Z. Peng, L. Tong, W. Shi, et al., "Multifunctional Human Visual Pathway-Replicated Hardware Based on 2D Materials," *Nature Communications* 15 (2024): 8650, https://doi.org/10.1038/s41467-024-52982-3.

16. X. Liu, D. Wang, W. Chen, et al., "Optoelectronic Synapses With Chemical-Electric Behaviors in Gallium Nitride Semiconductors for Biorealistic Neuromorphic Functionality," *Nature Communications* 15 (2024): 7671, https://doi.org/10.1038/s41467-024-51194-z.

17. W. Zeng, Z. Duan, Y. Bu, et al., "A Self-Powered HgTe Quantum Dots/PBDB-T:Y6 Bipolar Broadband Photodetector for Logic Gates," *Materials Horizons* 12 (2025): 2179–2186, https://doi.org/10.1039/d4mh01925c.

18. W. Zeng, Z. Duan, Y. Bu, et al., "Advances in Bipolar Photodetectors: Working Principles, Constructions, and Applications," *Laser & Photonics Reviews* 19 (2025): 2402163, https://doi.org/10.1002/lpor.202402163.

19. L. Pi, P. Wang, S.-J. Liang, et al., "Broadband Convolutional Processing Using Band-Alignment-Tunable Heterostructures," *Nature Electronics* 5 (2022): 248–254, https://doi.org/10.1038/s41928-022-00747-5.

20. Y. Bu, Y. Jiang, Z. Duan, et al., "Oriented Crystallization of HgTe Quantum Dots With Low Urbach Band-Tail for Broadband Optoelectronic Logic Gates," *Advanced Optical Materials* 13 (2025): 2500295, https://doi.org/10.1002/adom.202500295.

21. C. Fuentes-Hernandez, W.-F. Chou, T. M. Khan, et al., "Large-Area Low-Noise Flexible Organic Photodiodes for Detecting Faint Visible Light," *Science* 370 (2020): 698–701, https://doi.org/10.1126/science.aba2624.

22. N. Matsuhisa, S. Niu, S. J. K. O'Neill, et al., "High-Frequency and Intrinsically Stretchable Polymer Diodes," *Nature* 600 (2021): 246–252, https://doi.org/10.1038/s41586-021-04053-6.

23. B. Ouyang, J. Wang, G. Zeng, et al., "Bioinspired In-Sensor Spectral Adaptation for Perceiving Spectrally Distinctive Features," *Nature Electronics* 7 (2024): 705–713, https://doi.org/10.1038/s41928-024-01208-x.

24. L. Gu, S. Poddar, Y. Lin, et al., "A Biomimetic Eye With a Hemispherical Perovskite Nanowire Array Retina," *Nature* 581 (2020): 278–282, https://doi.org/10.1038/s41586-020-2285-x.

25. K. Liao, Y. Lian, M. Yu, et al., "Hetero-Integrated Perovskite/Si_3N_4 On-Chip Photonic System," *Nature Photonics* 19 (2025): 358–368, https://doi.org/10.1038/s41566-024-01603-y.

26. H. Huang, X. Liang, Y. Wang, et al., "Fully Integrated Multi-Mode Optoelectronic Memristor Array for Diversified In-Sensor Computing," *Nature Nanotechnology* 20 (2025): 93–103, https://doi.org/10.1038/s41565-024-01794-z.

27. Y. Chen, H. Wang, F. Luo, V. Montes-García, Z. Liu, and P. Samorì, "Nanofloating Gate Modulated Synaptic Organic Light-Emitting Transistors for Reconfigurable Displays," *Science Advances* 8 (2022): abq4824, https://www.science.org/doi/abs/10.1126/sciadv.abq4824.

28. N. Ding, W. Xu, H. Liu, et al., "Highly DUV to NIR-II Responsive Broadband Quantum Dots Heterojunction Photodetectors by Integrating Quantum Cutting Luminescent Concentrators," *Light: Science & Applications* 13 (2024): 289, https://doi.org/10.1038/s41377-024-01604-0.

29. S. Li, Y. Zhang, W. Yang, H. Liu, and X. Fang, "2D Perovskite $Sr_2Nb_3O_{10}$ for High-Performance UV Photodetectors," *Advanced Materials* 32 (2020): 1905443, https://doi.org/10.1002/adma.201905443.

30. Z. Li, T. Yan, and X. S. Fang, "Low-Dimensional Wide-Bandgap Semiconductors for UV Photodetectors," *Nature Reviews Materials* 8 (2023): 587–603, https://doi.org/10.1038/s41578-023-00583-9.

31. Y. Zhu, Y. Wang, X. Pang, et al., "Non-Volatile 2D MoS_2/Black Phosphorus Heterojunction Photodiodes in the Near- to Mid-Infrared Region," *Nature Communications* 15 (2024): 6015, https://doi.org/10.1038/s41467-024-50353-6.

32. Y. Chen, B. Han, M. Gobbi, L. Hou, and P. Samorì, "Responsive Molecules for Organic Neuromorphic Devices: Harnessing Memory Diversification," *Advanced Materials* 37 (2025): 2418281, https://advanced.onlinelibrary.wiley.com/doi/abs/10.1002/adma.202418281.

33. Y. Zhou, Z. Guo, H. Gu, et al., "A Solution-Processable Natural Crystal With Giant Optical Anisotropy for Efficient Manipulation of Light Polarization," *Nature Photonics* 18 (2024): 922–927, https://doi.org/10.1038/s41566-024-01461-8.

34. G. Wu, X. Zhang, G. Feng, et al., "Ferroelectric-Defined Reconfigurable Homojunctions for In-Memory Sensing and Computing," *Nature Materials* 22 (2023): 1499–1506, https://doi.org/10.1038/s41563-023-01676-0.

35. S. Li, X. Liu, H. Yang, H. Zhu, and X. Fang, "Two-Dimensional Perovskite Oxide as a Photoactive High-κ Gate Dielectric," *Nature Electronics* 7 (2024): 216–224, https://doi.org/10.1038/s41928-024-01129-9.

36. Y. Ma, L. Shan, Y. Ying, et al., "Day-Night Imaging Without Infrared Cutfilter Removal Based on Metal-Gradient Perovskite Single Crystal Photodetector," *Nature Communications* 15 (2024): 7516, https://doi.org/10.1038/s41467-024-51762-3.

37. L. Min, H. Sun, L. Guo, et al., "Frequency-Selective Perovskite Photodetector for Anti-Interference Optical Communications," *Nature*

15214095, 0, Downloaded from https://advanced.onlinelibrary.wiley.com/doi/10.1002/adma.75139 by Fudan University, Wiley Online Library on [04/10/2026]. See the Terms and Conditions (https://onlinelibrary.wiley.com/terms-and-conditions) on Wiley Online Library for rules of use; OA articles are governed by the applicable Creative Commons License

Communications 15 (2024): 2066, https://doi.org/10.1038/s41467-024-46468-5.

38. T. Guo, S. Li, Y. N. Zhou, W. D. Lu, Y. Yan, and Y. A. Wu, "Interspecies-Chimera Machine Vision With Polarimetry for Real-Time Navigation and Anti-Glare Pattern Recognition," *Nature Communications* 15 (2024): 6731, https://doi.org/10.1038/s41467-024-51178-z.

39. Z. Zhao, Z. Hu, M. Deng, et al., "Bias-Switchable Photodetection and Photosynapse Dual-Functional Devices Based on 2D Perovskite/Organic Heterojunction for Imaging-to-Recognition Conversion," *Advanced Materials* 37 (2025): 2416033, https://advanced.onlinelibrary.wiley.com/doi/abs/10.1002/adma.202416033.

40. J. Chen, X. Liu, Q. Zhu, X. Fang, and W. Xu, "2D $Ca_2Nb_3O_{10}$ Optoelectronic Neuromorphic Device for Ultrasensitive UV-C Vision and Encrypted Communication," *Advanced Functional Materials* 34 (2024): 2402684, https://advanced.onlinelibrary.wiley.com/doi/abs/10.1002/adfm.202402684.

41. S. Goffri, C. Müller, N. Stingelin-Stutzmann, et al., "Multicomponent Semiconducting Polymer Systems With Low Crystallization-Induced Percolation Threshold," *Nature Materials* 5 (2006): 950–956, https://doi.org/10.1038/nmat1779.

42. M. Campoy-Quiles, T. Ferenczi, T. Agostinelli, et al., "Morphology Evolution via Self-Organization and Lateral and Vertical Diffusion in Polymer:Fullerene Solar Cell Blends," *Nature Materials* 7 (2008): 158–164, https://doi.org/10.1038/nmat2102.

43. D. A. Vithanage, A. Devizis, V. Abramavicius, et al., "Visualizing Charge Separation in Bulk Heterojunction Organic Solar Cells," *Nature Communications* 4 (2013): 2334, https://doi.org/10.1038/ncomms3334.

44. F. Gao and O. Inganäs, "Charge Generation in Polymer–Fullerene Bulk-Heterojunction Solar Cells," *Physical Chemistry Chemical Physics* 16 (2014): 20291–20304, https://doi.org/10.1039/C4CP01814A.

45. A. J. Gillett, C. Tonnelé, G. Londi, et al., "Spontaneous Exciton Dissociation Enables Spin State Interconversion in Delayed Fluorescence Organic Semiconductors," *Nature Communications* 12 (2021): 6640, https://doi.org/10.1038/s41467-021-26689-8.

46. P. Zubko, G. Catalan, and A. K. Tagantsev, "Flexoelectric Effect in Solids," *Annual Review of Materials Research* 43 (2013): 387–421, https://www.annualreviews.org/content/journals/10.1146/annurev-matsci-071312-121634.

47. S. I. Rich, S. Lee, K. Fukuda, and T. Someya, "Developing the Non-developable: Creating Curved-Surface Electronics From Nonstretchable Devices," *Advanced Materials* 34 (2022): 2106683, https://doi.org/10.1002/adma.202106683.

48. H. Wang, S. Jin, X. Zhang, and Y. Xie, "Excitonic Effects in Polymeric Photocatalysts," *Angewandte Chemie International Edition* 59 (2020): 22828–22839, https://onlinelibrary.wiley.com/doi/abs/10.1002/anie.202002241.

49. R. H. Masland, "The Fundamental Plan of the Retina," *Nature Neuroscience* 4 (2001): 877–886, https://doi.org/10.1038/nn0901-877.

50. J. A. Movshon and P. Lennie, "Pattern-Selective Adaptation in Visual Cortical Neurones," *Nature* 278 (1979): 850–852, https://doi.org/10.1038/278850a0.

51. F. A. Dunn, M. J. Lankheet, and F. Rieke, "Light Adaptation in Cone Vision Involves Switching Between Receptor and Post-Receptor Sites," *Nature* 449 (2007): 603–606, https://doi.org/10.1038/nature06150.

52. L. Li, S. Li, W. Wang, et al., "Adaptative Machine Vision With Microsecond-Level Accurate Perception Beyond Human Retina," *Nature Communications* 15 (2024): 6261, https://doi.org/10.1038/s41467-024-50488-6.

53. T. Zhou, *Encyclopedia of Systems Biology*, ed. W. Dubitzky, O. Wolkenhauer, K.-H. Cho, and H. Yokota (Springer, 2013), https://doi.org/10.1007/978-1-4419-9863-7.

54. Z. He, H. Shen, D. Ye, et al., "An Organic Transistor With Light Intensity-Dependent Active Photoadaptation," *Nature Electronics* 4 (2021): 522–529, https://doi.org/10.1038/s41928-021-00615-8.

55. T.-J. Lee, K.-R. Yun, S.-K. Kim, et al., "Realization of an Artificial Visual Nervous System Using an Integrated Optoelectronic Device Array," *Advanced Materials* 33 (2021): 2105485, https://doi.org/10.1002/adma.202105485.

56. W. Liu, X. Yang, Z. Wang, et al., "Self-Powered and Broadband Opto-Sensor With Bionic Visual Adaptation Function Based on Multilayer γ-InSe Flakes," *Light: Science & Applications* 12 (2023): 180, https://doi.org/10.1038/s41377-023-01223-1.

57. W. Wen, G. Liu, X. Wei, et al., "Biomimetic Nanocluster Photoreceptors for Adaptative Circular Polarization Vision," *Nature Communications* 15 (2024): 2397, https://doi.org/10.1038/s41467-024-46646-5.

58. J. Zhu, W. Liu, W. Huang, et al., "Full Vision Adaptation in Mixed-Light Conditions Enabled by Dynamic Water Adsorption/Desorption," *Nature Communications* 17 (2026): 4965, https://doi.org/10.1038/s41467-026-73217-7.

59. L. Liu, F. Hu, J. Han, et al., "Adaptive Tunneling Photodiodes Enable Visual Recognition in High-Contrast Scenes," *Science Advances* 12 (2026): aec4849, https://doi.org/10.1126/sciadv.aec4849.

60. Z. Zhong, Y. Zhuang, X. Cheng, et al., "Ionic-Electronic Photodetector for Vision Assistance With In-Sensor Image Processing," *Nature Communications* 16 (2025): 7096, https://doi.org/10.1038/s41467-025-62563-7.

61. A. Nawaz, M. S. Meruvia, D. L. Tarange, et al., "High Mobility Organic Field-Effect Transistors Based on Defect-Free Regioregular Poly(3-hexylthiophene-2,5-diyl)," *Organic Electronics* 38 (2016): 89–96, https://www.sciencedirect.com/science/article/pii/S1566119916303408.

62. J. E. Anthony, A. Facchetti, M. Heeney, S. R. Marder, and X. Zhan, "n-Type Organic Semiconductors in Organic Electronics," *Advanced Materials* 22 (2010): 3876–3892, https://doi.org/10.1002/adma.200903628.

63. D. P. Kingma and J. Ba, "Adam: A Method for Stochastic Optimization," International Conference on Learning Representations (2014), https://doi.org/10.48550/arXiv.1412.6980, CoRR abs/1412.6980.

64. A. Paszke, S. Gross, F. Massa, et al., "PyTorch: An Imperative Style, High-Performance Deep Learning Library," (2019), https://doi.org/10.48550/arXiv.1912.01703, ArXiv abs/1912.01703.

Supporting Information

Additional supporting information can be found online in the Supporting Information section.

Supporting File: adma75139-sup-0001-SuppMat.docx.

15214095, 0, Downloaded from https://advanced.onlinelibrary.wiley.com/doi/10.1002/adma.75139 by Fudan University, Wiley Online Library on [04/10/2026]. See the Terms and Conditions (https://onlinelibrary.wiley.com/terms-and-conditions) on Wiley Online Library for rules of use; OA articles are governed by the applicable Creative Commons License